



Preparation and Performance of Ni-Al and 3Cr13 Coatings on Carbon Steel by Arc Spraying for Boiler Heat Exchanger Pipelines: A Comparative Study

Yicheng Zhou¹ · Wangping Wu¹ · Jiaqi Huang¹ · Guoqing Sun¹ · Guang He¹ ·
Yusheng Jiang¹ · Yi Zhang^{1,2} · Zhizhi Wang¹ · Yaxuan Liu¹ · Shuangcheng Fu^{1,2} ·
Peng Jiang¹ · Guofu Ou^{2,3}

Submitted: 20 June 2022 / in revised form: 3 November 2022 / Accepted: 9 November 2022 / Published online: 28 December 2022
© ASM International 2022

Abstract This study compares nickel-aluminum (Ni-Al) and 3Cr13 steel coatings deposited on carbon steel substrates by arc spraying. The objective is to select a coating that will improve the corrosion and abrasion wear resistance of boiler heat exchanger pipes. This comparison involves the study of the microstructure, phase composition, microhardness, wear and erosion, and corrosion resistance of the coatings. The corrosion resistance was evaluated based on seawater immersion, electrochemical impedance, polarization, and galvanic corrosion tests. The results showed that the Ni-Al coating had a porosity of 6.3%, while the 3Cr13 coating had a porosity of 5.2%. The average surface roughness of the 3Cr13, Ni-Al coatings, and polished substrate were 11, 14.4, and 0.13 μm , respectively. The 3Cr13 lamellar structure coating was mainly composed of the α -Fe phase and a small amount of the CrO phase, and the Ni-16wt%Al coating included a solid solution phase and a small amount of the NiO phase. During the wear tests, the Cr13 steel coating had the highest microhardness and the best abrasion resistance at room temperature at the initial stage of friction. However, its abrasion resistance was lower than that of the Ni-Al coating after a 10-min friction test. The friction coefficients

of the two coatings were almost the same at 300 °C. The corrosion resistance of the Ni-Al coating was better than that of the 3Cr13 steel coating. The current density of galvanic corrosion of the 3Cr13 coating was 108 $\mu\text{A m}^{-2}$ and that of the Ni-Al coating was 37 $\mu\text{A cm}^{-2}$, indicating that galvanic corrosion occurred between the substrate and the coating. This comparison showed that the Ni-Al coating could provide better high-temperature abrasion resistance and anti-corrosion performance for boiler heat exchanger piping compared with the 3Cr13 steel coating.

Keywords 3Cr13 steel coating · abrasion-resistant coating · arc spraying · coating · corrosion-resistant coating · Ni-Al coating

Introduction

The high-temperature corrosion and abrasion of boilers under corrosive gas flow and particle erosion environments seriously affect the safe operation and result in huge economic losses (Ref 1). To solve this issue, it is necessary to find a reliable, economic, and effective coating to improve the surface quality of the boiler tube wall, thus prolonging the service life of the equipment (Ref 2). In this way, the occurrence of accidents can be minimized, and the reliability and safety of the boiler is improved. Surface coating technology is an effective way to solve this problem (Ref 3-5).

Thermal spraying is an effective and low-cost coating method that is applied as thick coatings to change the surface properties of the components (Ref 6). The deposition efficiency of the process is very high, and the coating adhesion is also adequate (Ref 7-9). It has the advantages of simple equipment and low cost, and is suitable for on-

✉ Wangping Wu
wup3.14@163.com; wuwping@cczu.edu.cn

¹ Electrochemistry and Corrosion Laboratory, School of Mechanical Engineering and Rail Transit, Changzhou University, Changzhou 213164, People's Republic of China

² School of Mechanical Engineering and Rail Transit, Changzhou University, Changzhou 213164, People's Republic of China

³ Institute of Flow-Induced Corrosion and Intelligent Prevention and Control, Changzhou University, Changzhou 213164, China

site operation, especially for the protection, repair, and remanufacturing of large equipment, such as boiler heating surface tubes. It is also a direct and effective method with a remarkable resource-saving effect (Ref 10, 11). The applications of thermal spraying technology include aircraft engines (Ref 12), transportation (Ref 13), automotive systems (Ref 14), petrochemical process equipment (Ref 15), marine turbines (Ref 16, 17), and power generation equipment (Ref 18).

In everyday practice, robust and easy-to-use processes, such as arc spraying, or powder flame spraying are often used alongside highly developed kinetic spray processes (Ref 19–21). Fauchais et al. (Ref 22) studied the spraying process of the coatings. Wire spraying technology mainly includes arc spraying, wire flame spraying, and plasma transfer arc spraying. For spraying cored wire and solid wire, arc spraying and flame spraying are mature, low-cost methods. However, the as-prepared coating is seriously oxidized and has high porosity. As a new wire spraying process, plasma transferred wire arc spraying has a low oxidation degree for the coating, low porosity, and good coating quality, but the cost is high. The main methods of improving coating quality are to optimize the spraying process, and to design new spraying technology by studying the melting mechanism and droplet characteristics of wire during the spraying process (Ref 23). Therefore, arc spraying is mostly used in large area spraying projects of boiler heating pipes and air- and water-cooled walls. Recently, Ni–Al alloys have been adopted by industry for high-temperature oxidation corrosion and erosion coatings (Ref 24, 25). Thermally-sprayed Ni-based alloy coatings can provide many benefits for industrial applications. In particular, resistance to wear, corrosion, and oxidation is required for protection of the components (Ref 26, 27). There are various Ni-based alloy coatings, such as Ni–20Cr (Ref 28), Inconel 625 (Ref 29, 30), and Hastelloy C276 (Ref 31), which are commonly used for wear- and corrosion-resistant coatings in severe environments. In addition, 3Cr13 stainless steel is also a candidate for abrasion- and corrosion-resistant coatings (Ref 17), and is the most widely used in mechanical manufacturing. 3Cr13 stainless steel has a high Cr mass fraction and high strength and hardness, and is mainly used for instruments requiring high hardness and abrasion and corrosion resistance (Ref 32–36).

Consequently, in this study, Ni–Al and 3Cr13 coatings were prepared on the surface of carbon steel substrates by arc spraying, in order to apply the selected coating as a protective barrier for boiler heating pipelines, which should meet a requirement in simultaneously enhancing the abrasion resistance and anticorrosion performance. For this purpose, the microstructure, surface roughness, phases, and chemical composition of the coatings were analyzed and

studied. At the same time, the microhardness and the abrasion and corrosion resistance of the coatings were compared and further investigated.

Experimental

Preparation

Carbon steel Q235 (size: 300 × 27 × 3 mm) was used as the substrate. The chemical composition of the spraying materials and the substrate is shown in Table 1. The coating was sprayed using an industrial arc-spray system (ARC 9000; TAFE, Concord, NH, USA). The coating materials were nickel-aluminum alloy wire (Ni–16wt%Al) and 3Cr13 steel wire with a diameter of 2 mm, provided by Shanghai HanBo. Table 2 displays the deposition parameters of the arc-spraying process. The digital images of the two coatings on carbon steel substrates are displayed in Fig. 1. In preparation for the arc-sprayed coatings, the surface of the substrate was sandblasted with corundum Al₂O₃ white irregular-shaped particles with the size of about 100–125 μm, in order to improve the surface roughness of the substrate, and enhance the adhesion of the coating to the substrate due to the effect of mechanical locking.

Characterizations

The samples sprayed with the coatings were cut by a wire-cutting machine, and the surface of the sample was washed with acetone in order to observe the morphology and microstructure of the top surface and cross-section of the coatings on the substrate. The treated samples were mounted with epoxy resin in a small mold and then cured. The cross-section of the coating was polished with metallographic abrasive paper (5–20 μm), then by a 1-μm diamond solution, and finally by a 0.3-μm alumina suspension.

The surface roughness of the coating was evaluated by an optical profilometer (Contourgt K0; Bruker, Karlsruhe, Germany). An optical microscope with an ultra-depth 3D

Table 1 Chemical composition of material (mass fraction)

Material	Chemical composition, wt%								
	C	Mn	Si	S	P	Cr	Ni	Al	Fe
Q235	0.20	1.4	0.35	0.045	0.045	97.96
Ni–Al	84	16	
3Cr13	0.35	1.00	1.00	0.03	0.035	14	0.6	...	82.98

microscope system (VHX-700FC; KEYENCE, Osaka, Japan) was used to observe the surface morphology of the coating. The microstructure and morphology of the surface and the cross-section of the coatings were analyzed by scanning electronic microscopy (SEM; Sigma 500; ZEISS, Oberkochen, Germany) at $\times 300$, $\times 500$, and $\times 1000$ magnifications with an in-lens backscatter detector, with an acceleration voltage of 20 kV. ImageJ software was used to calculate the porosity of the coatings. The coating thicknesses were measured at five points on the cross-section of the SEM images. The phase identification and grain orientation of the coatings were analyzed by x-ray diffraction (XRD; D-MAX 2500, Rigaku, Tokyo, Japan) using monochromatic Cu K α radiation ($\lambda = 1.5406 \text{ \AA}$).

Microhardness

The microhardness of the coatings on the carbon steel substrate was measured by a Vickers microhardness tester (HMV-2000; SHIMADZU, Kyoto-fu, Japan) under 5-N load for a penetration time of 15 s, and the final value for each specimen was averaged from five indentations. Simultaneously, the morphology of the indentation was observed by optical microscopy (VHX-700FC; KEYENCE).

Table 2 Arc-spraying process parameters

Coatings	Ni-Al	3Cr13
Spray voltage, V	30	30
Spray current, A	200	200
Spray angle, °	90	90
Spray distance, mm	150	150
Atomized gas (air) pressure, MPa	0.5	0.5
Spray gun movement speed, mm/s	200	200

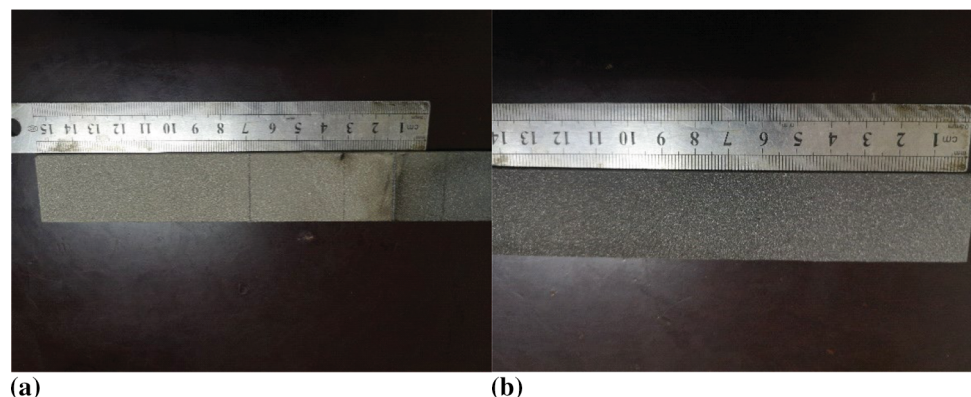
Abrasion Resistance

The abrasion resistance of the coating was determined by a material surface property tester (CFT-1; Zhongke Kaihua, Lanzhou, China) at room temperature, under the load of 2 N, grinding ball material of Si₃N₄, a reciprocating stroke of 4 mm, and a friction speed of 400 rpm for 15 min. For high-temperature abrasion, the abrasion resistance of the coating was determined by high-temperature friction and wear tester (HT-1000; Zhongke Kaihua) at the high temperature of 300 °C under the load of 2 N, grinding ball material of Si₃N₄, friction radius of 3 mm, motor speed of 500 rpm, and the test was performed for 15 min.

Corrosion Resistance

Using a weight loss method, the corrosion rate of the two coatings was calculated and their corrosion resistance was analyzed after soaking in 3.5 wt% sodium chloride (NaCl) solution for 4 months. The corrosion resistance of the coatings and the substrate were studied by a polarization test, using an electrochemical workstation (CHI660E; Chen Hua, Shanghai, China). The coating on the substrate as the working electrode was affixed to a copper conductive wire, and then manually coated with epoxy resin, leaving a geometrical surface area of 1 cm² exposed to 3.5 wt% NaCl solution. There was a three-compartment electrode, an Ag/AgCl 3 M KCl as the reference electrode and a Pt electrode (size: 15 × 15 × 0.5 mm) as the counter electrode. The electrochemical test was recorded at a sweep rate of 10 mV s⁻¹ at room temperature, and the steady-state open circuit potential (OCP) for each specimen was carried out for 30 min. Before the polarization test, electrochemical impedance spectroscopic (EIS) measurements were carried out at the measured steady-state OCP value of the corresponding working electrode in the frequency range of 10⁻²–10⁵ Hz. Meanwhile, the current corrosion density (i_{corr}) was calculated by the Stern–Geary formula

Fig. 1 Digital images of arc-sprayed coatings on carbon steel substrates: (a) Ni-Al coating and (b) 3Cr13 coating



(Eq. 1), and the corrosion rate was calculated by the Faraday formula (Eq. 2) (Ref 37):

$$i_{\text{corr}} = \frac{\beta_a \times \beta_c}{(2.303R_p)(\beta_a + \beta_c)} \quad (\text{Eq 1})$$

$$\text{CR} = \frac{3270 \times M \times i_{\text{corr}}}{\rho \times Z} \quad (\text{Eq 2})$$

i_{corr} Current corrosion density, A/cm²

R_p Polarization resistance, Ω · cm²

β_a Anode slope

β_c Cathode slope

CR Cathode slope, mil/year

M Relative atomic mass of metal

ρ Metal density, g/cm³

Z Reaction transferred electrons

The galvanic corrosion potential between the coating and the substrate as the galvanic couple pair was tested with a double-electrode mode and open-circuit voltage for 9 h by an electrochemical workstation, which was immersed in a 3.5 wt% NaCl solution with the volume of 150 mL. The size of the sample was 27 × 27 × 3 mm. The galvanic corrosion current between the coating and the substrate was tested with a three-electrode mode and the current–time curve was selected; the galvanic corrosion principle and experimental apparatus are shown in Fig. 2. Experiments were carried out for 9 h to determine the corrosion at different current densities. The galvanic corrosion samples were the Ni-Al alloy coating and the 3Cr13

coating, respectively, and base carbon steel was used as the galvanic couple pair. The two galvanic couples were connected by copper wire conductors and dipped separately. The corrosion state of the coating was observed after immersion for 7 days. Table 3 displays the material contact sensitivity coefficient evaluation criteria.

Results and Discussion

Characterization

Micromorphology of the Coating Surface

Figure 3 shows the 2D and 3D optical micrographs of the Ni-Al alloy and 3Cr13 steel coatings. The surface of the coatings was rough, and some large particles were present (Fig. 3a and c), which is attributed to the process of arc spraying. In Fig. 3(b) and (d), the highest peak values of the Ni-Al and 3Cr13 coatings are 124.2 and 121.9 μm, respectively. Therefore, the surface roughness values of the arc-sprayed coatings were almost the same. It can be seen that some oxides (rusty spots) are present in Fig. 3c), which is due to the oxidation of the fusion particles during the spraying process in air at atmospheric pressure.

Surface Roughness

Figure 4 shows the 3D optical micrographs of the surface of the coatings and the substrate. The contour arithmetic mean deviation (Ra) of the 3Cr13 coating, the Ni-Al coating, and the polished substrate were 11 ± 0.20, 14.4 ± 0.22, and 0.13 ± 0.05 μm, respectively, indicating that the surface of the Ni-Al coating was slightly rougher than that of the 3Cr13 coating. It can be seen from Fig. 4(a) and (b) that the number of mountain peaks in the Ni-Al coating was many more than in the 3Cr13 coating. The polished substrate was smooth, but the rough surface of the substrate caused by sandblasting was not tested because it was too rough to measure the surface roughness.

Microstructure

Figure 5 shows the SEM images of the surface of the coatings. These were relatively rough due to the effect of the sandblasted substrate. In Fig. 5(a), the Ni-Al deposit is fine-grained, compact, continuous, and dense. The surface of Ni-Al coating is rough and uneven, the surface structure shape is similar to a wave. The surface contains a few independent oxidation particles, but it also contains few pores. After energy dispersive spectroscopy (EDS) pattern testing, the chemical composition of the Ni-Al coating was mainly composed of Ni and Al elements, and a small

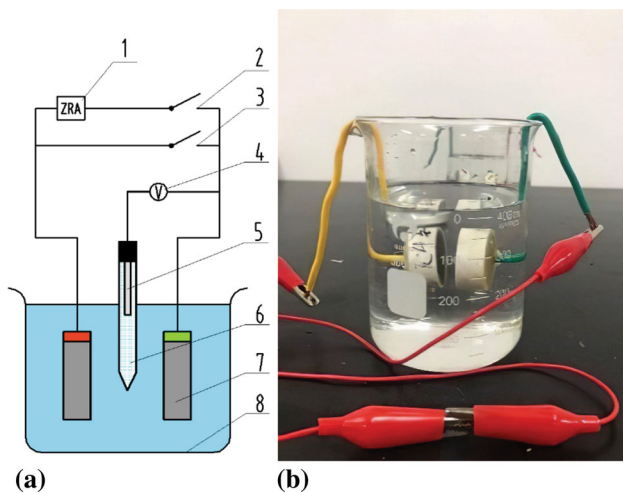
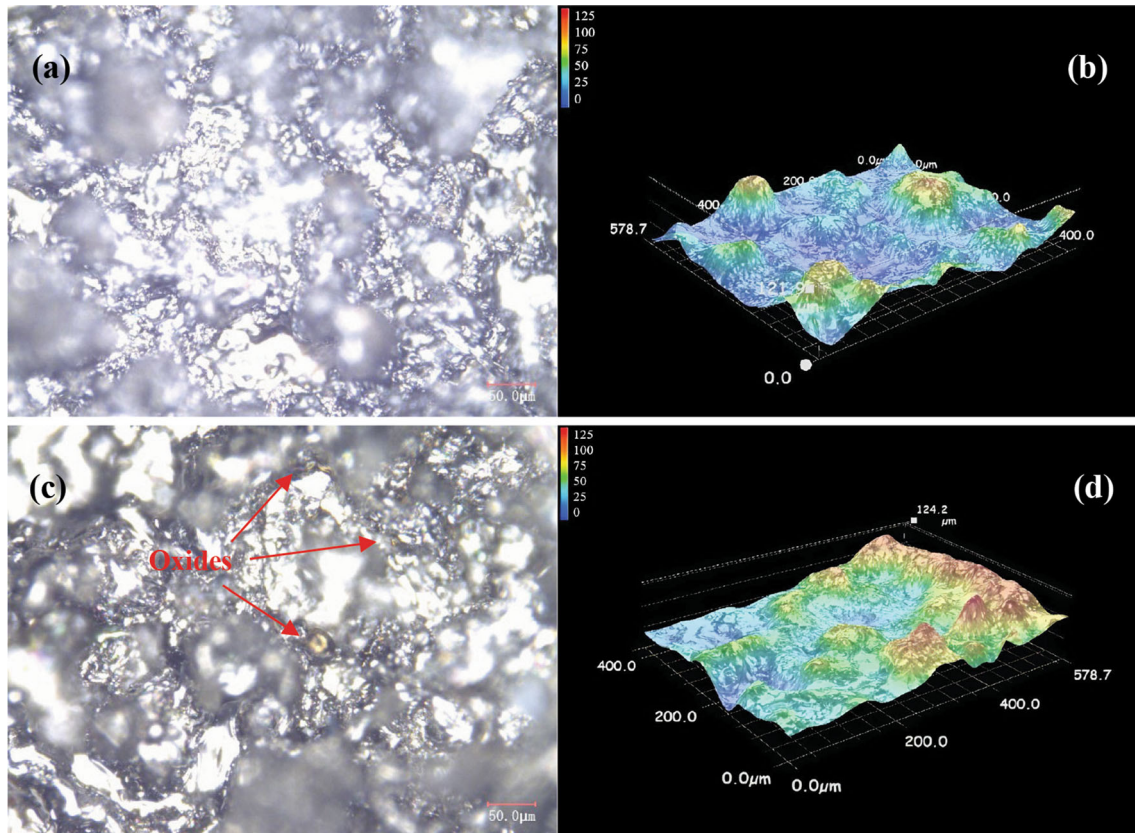


Fig. 2 Galvanic corrosion principle and actual test device: (a) galvanic corrosion principle (1 zero resistance ammeter, 2 switch, 3 switch, 4 multimeter, 5 reference electrode, 6 salt bridge, 7 tested sample, 8 beakers); (b) digital image of the conduction of galvanic couple

Table 3 Material contact sensitivity coefficient evaluation criteria (Ref 47)

No.	Current density ($\mu\text{A cm}^{-2}$)	Grade	Corrosion state	Condition of use
1	$I_g \leq 0.3$	A	No	Use directly
2	$0.3 < I_g \leq 1.0$	B	Slight	Conditional contract
3	$1.0 < I_g \leq 3.0$	C	Obvious	Use after protection
4	$3.0 < I_g \leq 10.0$	D	Medium	Use after protection
5	$I_{\text{avg}} > 10.0$	E	Severe	Use after protection

**Fig. 3** 2D and 3D optical micrographs of the coatings: (a, b) Ni-Al coating and (c, d) 3Cr13 coating

amount of oxygen. If just considering the Ni and Al elements, the coating was composed of $\sim 84\%$ wt% Ni and $\sim 16\%$ wt% Al, respectively. Figure 5(b) displays the SEM image of the surface of the 3Cr13 coating, which is not smooth enough as there are some circular protrusions, but the surface is flat, and no cracks or deep pits are visible. The coating is attached to some clusters and spherical nodules, but no obvious holes were observed. After EDS pattern testing, the chemical composition of the 3Cr13 coating comprised mainly Fe and Cr elements, and small amount of oxygen and carbon.

Figure 6 displays the SEM images of the cross-section of the coatings. The thickness of Ni-Al (Fig. 6a) and 3Cr13 coatings (Fig. 6b) is about 96.6 ± 4.6 and 177 ± 4.3 μm , respectively. The molten particles, which possess high kinetic energy, strike the substrate, and form a flat liquid

sheet under the impact force and solidify on the rough surface of the substrate to form a layered coating, so both coatings show a lamellar structure. In Fig. 6(b), the gray parts are Cr oxides, Cr-based carbides, and pores (Ref 38), the black parts are pores (Ref 39), and the light gray part is 3Cr13. The Ni-Al coating had a porosity of 6.28%, while the 3Cr13 coating had a porosity of 5.22%. Some oxides are observed in the coating because the spraying coating material was oxidized at high temperature during the spraying process. In addition, there are pores in the coating, which are formed by the deposition of particles of different sizes. The coatings display a wavy distribution because the wires were molten and the high-speed and high temperature droplets in the arc spray gun were sprayed under high-pressure gas, and impacted the surface of the substrate. For the 3Cr13 coating, some holes and pores were present at

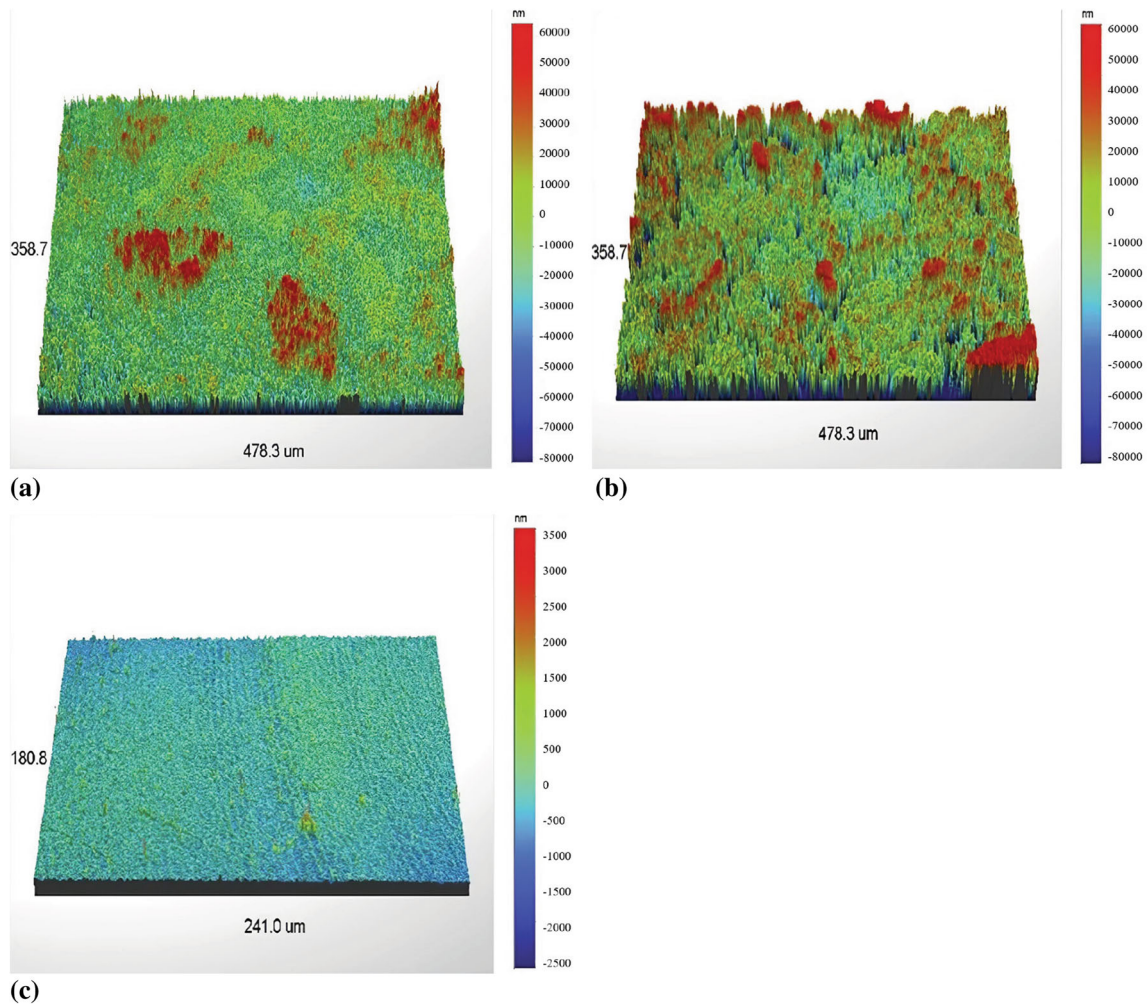
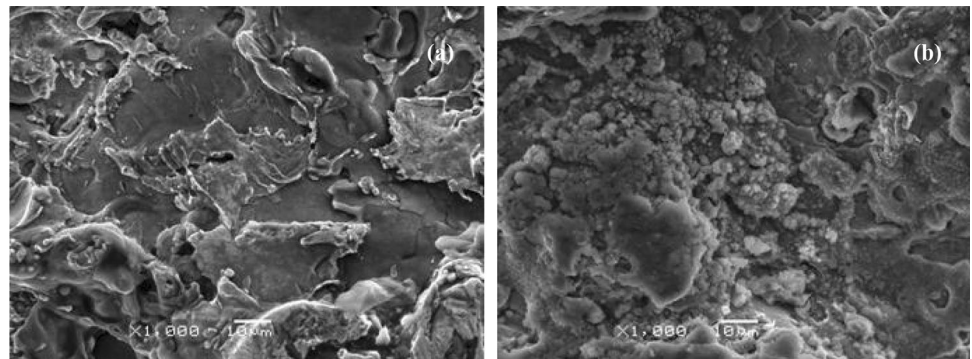


Fig. 4 3D optical micrographs of the surface of: (a) 3Cr13 coating, (b) Ni-Al coating, and (c) carbon steel polished substrate

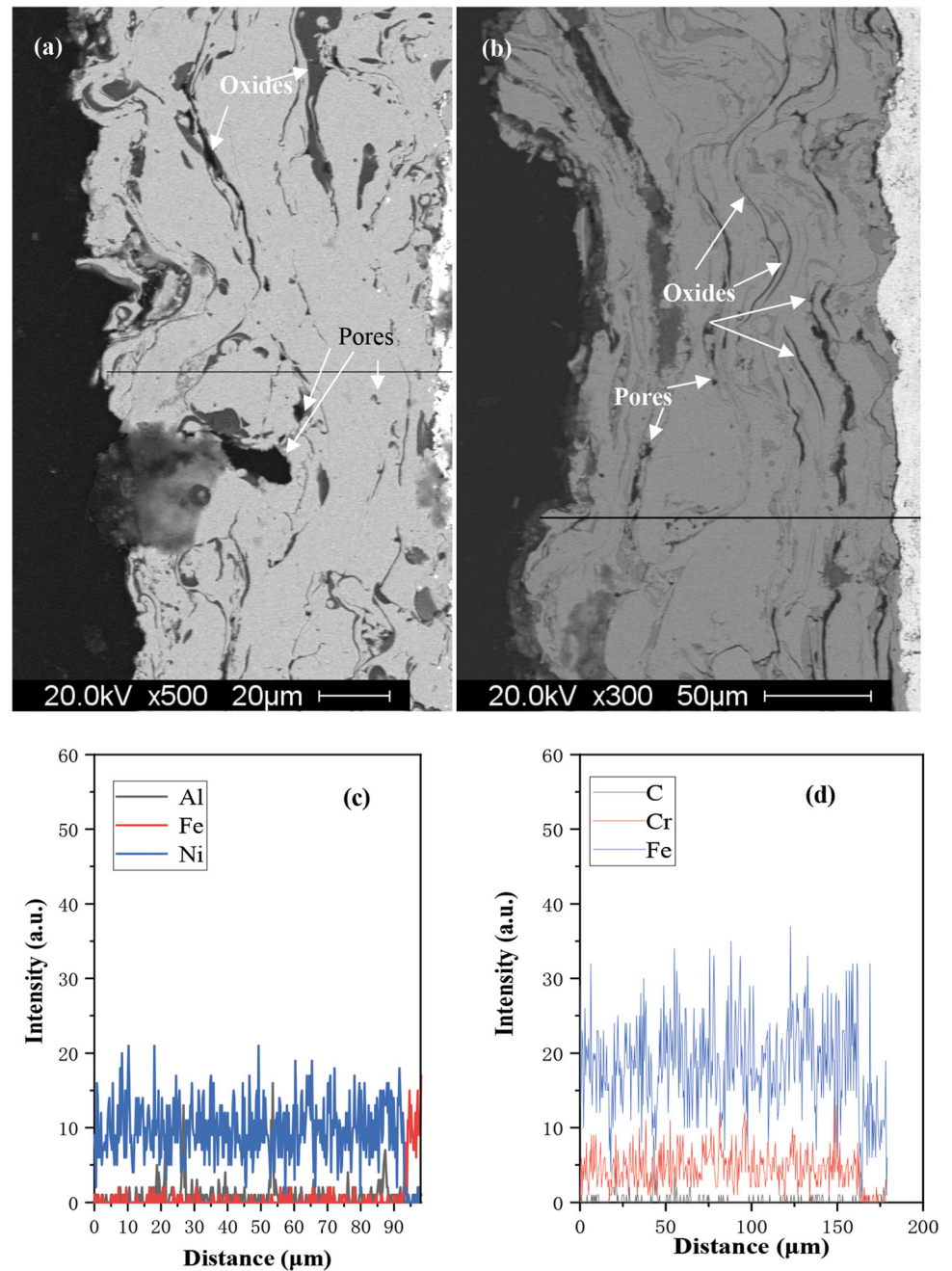
Fig. 5 SEM images of the top surface of: (a) Ni-Al and (b) 3Cr13 steel coatings



the interface between the coating and the substrate. It is possible for some fine sandblasted particles to be left on the substrate surface as impurities after the sandblasting. Additionally, the 3Cr13 coating has a higher hardness compared with the carbon steel substrate, resulting in the

shrinkage of the coating at the interface and the formation of porosity (Ref 40). The intimate contact between the coating and the substrate influences the adhesion, and some pores or holes at intimate contact points could possibly decrease the adhesion of the 3Cr13 coating. The line

Fig. 6 SEM images and line scanning analysis of Ni-Al and 3Cr13 coatings on carbon steel: (a) SEM image and (c) line scanning analysis of the Ni-Al coating, (b) SEM image and (d) line scanning analysis of the 3Cr13 coating



scanning analysis is illustrated in Fig. 6(c) and (d). The elements Fe, C, and Cr account for the majority of the content in the 3Cr13 coating, while the content of Ni in the Ni-Al alloy coating is much greater than that in the 3Cr13 coating. The cross-section of the 3Cr13 coating shows some gray and dark substances, which is due to some pores, carbides, and oxides which were formed during the arc-spraying process. The oxides formed in the coating influence the adhesion of the coating.

Crystallographic Phases

Figure 7 shows the XRD patterns of the 3Cr13 and Ni-Al coatings. According to the analysis of Jade software (PDF #06-0669), 3Cr13 coating was composed of a large number of α -Fe phase and a small amount of CrO phase (PDF#06-0532). The CrO oxide was formed because the fusion particles were oxidized from oxygen under air atmosphere during the arc spraying (Ref 33). The (110), (200), and (211) reflections of the α -Fe phase appear at 44.57°, 74°, and 82.17°, respectively, indicating that the as-sprayed

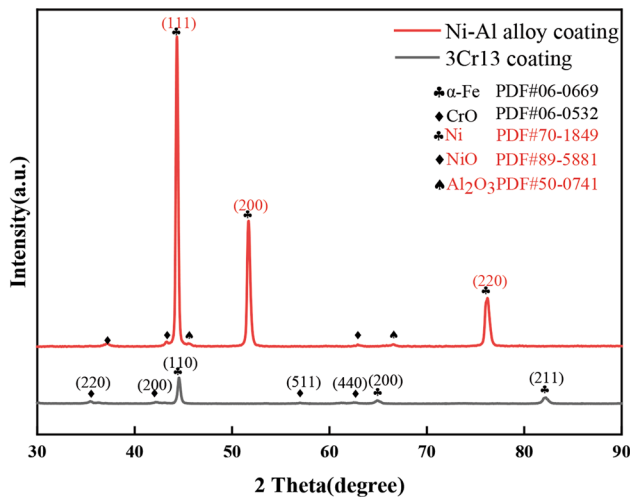


Fig. 7 XRD patterns of as-sprayed 3Cr13 and Ni-Al coatings

3Cr13 coating is a body-centered cubic (bcc) crystal structure. For the Ni-Al alloy coating, as the spraying material is a Ni-Al alloy wire, the content of Al in the wire is ~ 16 wt%, proved by the EDS pattern. Therefore, after the preparation of Ni-Al alloy coating, the coating was composed of Ni-Al solid solution. There are three diffraction peaks, (111), (200) and (220), corresponding to the Bragg angles of 44.4°, 51.8°, and 76.4°. It was worth noting that the diffraction peaks of Ni(111) and Ni(200) were slightly shifted toward a small 2-theta angle, compared to the standard Ni card, PDF #00-70-1849, indicating that a Ni-Al solid solution was formed. The atomic radius of Ni is 1.62 Å, while the atomic radius of Al is 1.82 Å, which is larger than Ni. When the Ni-Al alloy coating was obtained, Al entered the lattice site of Ni crystalline, resulting in the enlargement of the grain cell of Ni, and a shift of the diffraction peak to the left direction. In addition, it can be seen from Fig. 7 that there are very small diffraction peaks corresponding to the NiO phase of standard card PDF #00-89-5881 and the Al₂O₃ phase of standard card PDF #00-50-0741. These oxides are caused by the fact that the arc spraying was carried out under air atmosphere. Due to the high temperature generated in the spraying process, a small amount of Ni and Al molten particles was oxidized to form the oxides, such as NiO (Ref 41) and Al₂O₃ (Ref 42, 43).

Microhardness

Table 4 displays the average microhardness of the coating and the substrate. The microhardness values of the Ni-Al coating, 3Cr13 coating, and the substrate were 162.8 ± 12.64 HV_{0.5}, 446.5 ± 24.89 HV_{0.5}, and 177.0 ± 2.26 HV_{0.5}, respectively. The microhardness of the Ni-Al coating is close to that of carbon steel, but far

Table 4 Microhardness of the coatings and carbon steel substrate (HV_{0.5})

NO	Ni-Al alloy	3Cr13	Carbon steel
1	155.65	419.42	174.33
2	178.13	424.81	176.15
3	156.87	464.98	178.83
4	171.02	459.04	184.53
5	155.74	511.67	178.86
6	159.4	398.95	169.04
Average value	162.8	446.5	177.0
SD	12.64	24.89	2.26

less than that of the 3Cr13 coating. Figure 8 shows the optical micrographs of the indentations after the hardness test. The indentation of the 3Cr13 coating is significantly smaller than that of the carbon steel substrate and the Ni-Al coating, which also reflects that the hardness of the 3Cr13 coating was high. Starosta (Ref 44) studied the properties of thermally-sprayed Ni-5%Al, Ni-15%Al and Ni-25 ~ 35%Al alloy coatings and found that the more the Al-content in the alloy coating, the harder the coating. The microhardness of the Ni-25 ~ 35%Al alloy coatings resulted from the NiAl phase being about 250 HV_{0.04}. In this study, the microhardness of the Ni-16%Al coating is slightly less than that of the Ni-25%Al coating. The hardness of the low carbon steel is about 185 HV_{0.5} (Ref 45), and the microhardness of the 3Cr13 steel is about 450 HV_{0.5}. Compared to the other two materials, the microhardness of the 3Cr13 coating is much higher. On the one hand, the dense microstructure and low porosity contributes to an increase of the hardness. On the other hand, the stainless steel 3Cr13 is harder compared to the low carbon steel. The 3Cr13 coating is composed of hard phases (Fig. 6b), such as an Fe-Cr solid solution, which can take the role of a solid-solution strengthening effect, and Cr oxides, which can take a dispersion-strengthened effect (Ref 46, 47), which are beneficial for improving the microhardness.

Abrasion Resistance

The friction coefficients of the coatings are shown in Fig. 9. At the initial friction test stage, the friction coefficients of the Ni-Al and 3Cr13 coatings are about 0.4 and 0.28, respectively. The friction coefficient of the 3Cr13 coating is significantly lower than that of the Ni-Al coating. However, after friction testing for 3 min, the friction coefficient of the 3Cr13 coating suddenly increased sharply and exceeded that of the Ni-Al coating after 10 min. It can

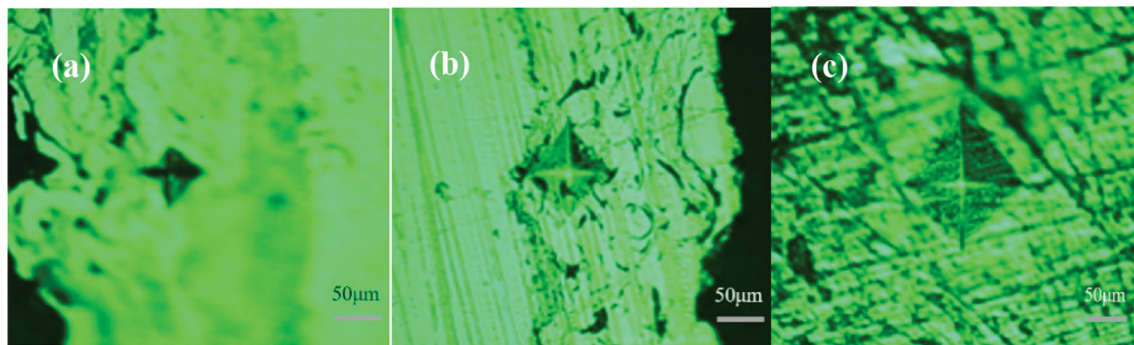


Fig. 8 Optical micrographs of microhardness indentations: (a) 3Cr13 coating, (b) Ni-Al coating, and (c) carbon steel substrate (magnification $\times 40$)

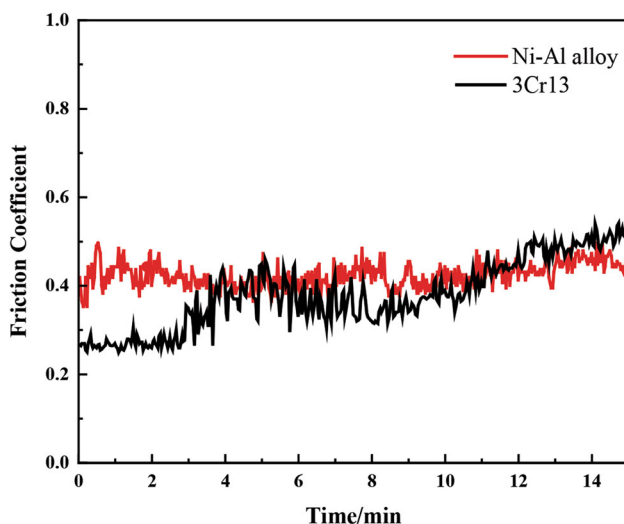


Fig. 9 Friction coefficients of the coatings and the substrate at room temperature

be inferred that there were poor interfaces between the laminated structure layers after the formation of many droplets due to the formation of oxides in the coating, as the grinding ball was loaded and reciprocated on the surface of the coating. The oxides were distributed in the coating, which will destroy the property of continuity and the cohesive strength of the coating. The poor interfaces between the layers resulted in the poor adhesion of the droplet-shaped layer, finally making the friction coefficient of the 3Cr13 coating increase after friction testing for 3 min. After the friction test, Fig. 10 shows the optical micrographs and contour profiles of the wear traces. We can see that the scratch width of the wear trace of the 3Cr13 coating is significantly greater than that of the Ni-Al coating (see Fig. 10(a) and (b)). As shown in Fig. 10(c), the depth and width of the 3Cr13 coating were 15.78 μm and 335.1 μm , respectively. However, in Fig. 10(d), the depth and width of the Ni-Al coating were 6.82 μm and 260.7 μm , respectively, indicating that the 3Cr13 coating has a deeper and wider scratch compared to the Ni-Al

coating. Therefore, the abrasion resistance of the Ni-Al coating was better than that of the 3Cr13 coating at room temperature.

Figure 11 displays the friction coefficients of the coatings at the high temperature of 300 $^{\circ}\text{C}$. The 3Cr13 coating has a slightly lower coefficient of friction than the Ni-Al coating. The friction coefficients of the 3Cr13 and Ni-Al coatings are about 1.145, and 1.158, respectively. Even though the Ni-Al coating has a slightly higher friction coefficient at high temperature, this coating provides better abrasion resistance than the 3Cr13 coating at room temperature.

Figure 12 shows the XRD patterns of the 3Cr13 and Ni-Al coatings after high-temperature friction testing. For the 3Cr13 coating, there was a diffraction peak in the vicinity of 2θ at about 44.57° . The α -Fe had a strong (111) reflection and two weak reflections of (200) and (220) appear at the Bragg angles of 44.57° , 74° , and 82.17° , respectively, before the high-temperature friction test, indicating that the crystal structure (bcc) of the 3Cr13 coating has not changed and that no oxide was found for iron. However, according to the analysis of Jade software, the Cr element is more easily oxidized to Cr_2O_3 at $> 600^{\circ}\text{C}$, and the Cr_2O_3 phase (PDF #85-0869) was formed after the high-temperature friction test (Ref 32, 48). The phase and texture of the Ni-Al solid-solution does not exhibit any new phases, and the location of the diffraction peaks was not changed significantly, indicating that the crystal phase Ni-Al coating is not changed. Therefore, the arc-sprayed Ni-Al alloy coating shows good high-temperature oxidation and abrasion resistance.

Figure 13 presents the optical 2D and 3D micrographs of the scratches on the coatings after high-temperature friction testing. At room temperature, the coatings are primarily subjected to abrasive and oxidative wear mechanisms. At the high temperature of 300 $^{\circ}\text{C}$, oxidation wear and adhesive wear were the predominant wear mechanisms. Abrasive grains were formed by the wear debris produced by the rupture of the oxide films and by the

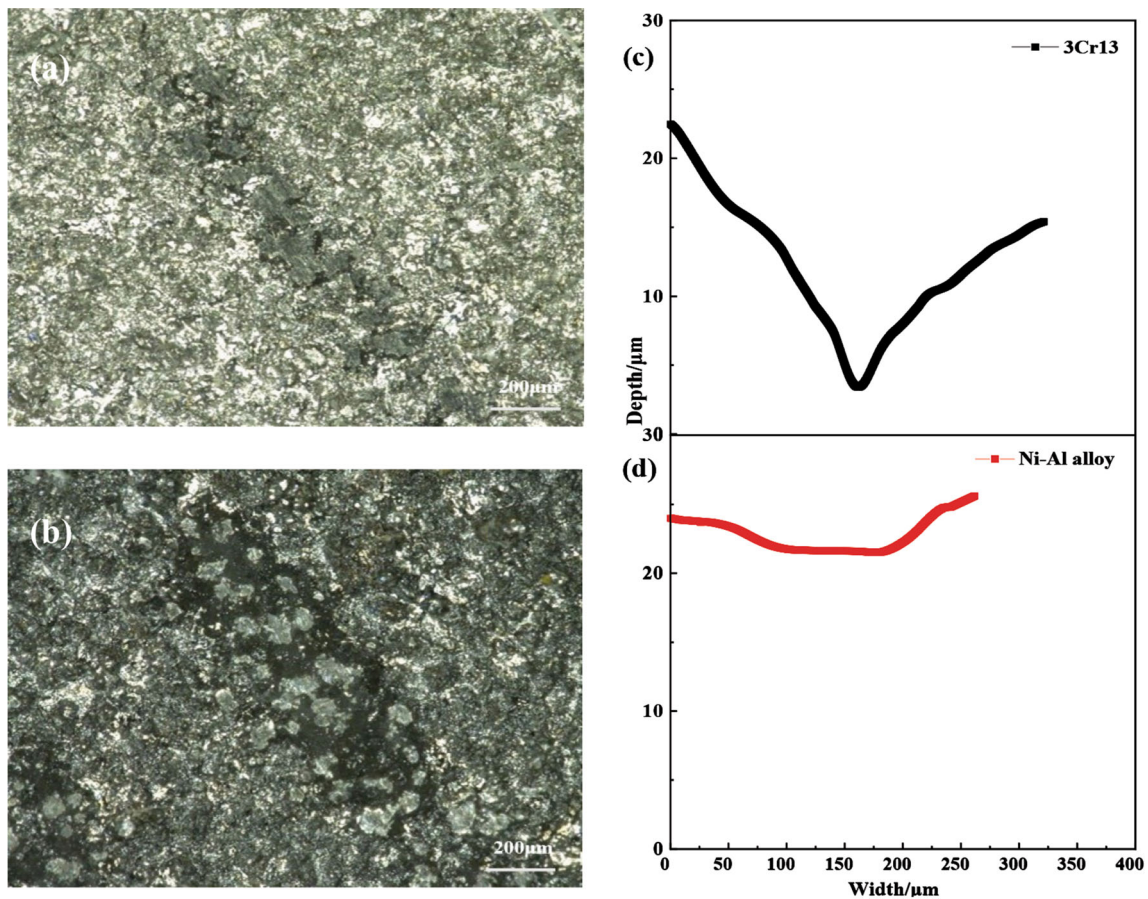


Fig. 10 Optical 2D micrographs of the scratches on the coatings after room-temperature friction testing: (a) Ni-Al coating, (b) 3Cr13 coating, (c) contour profiles of the groove for the 3Cr13 coating, (d) contour profiles of the groove for the vNi-Al coating

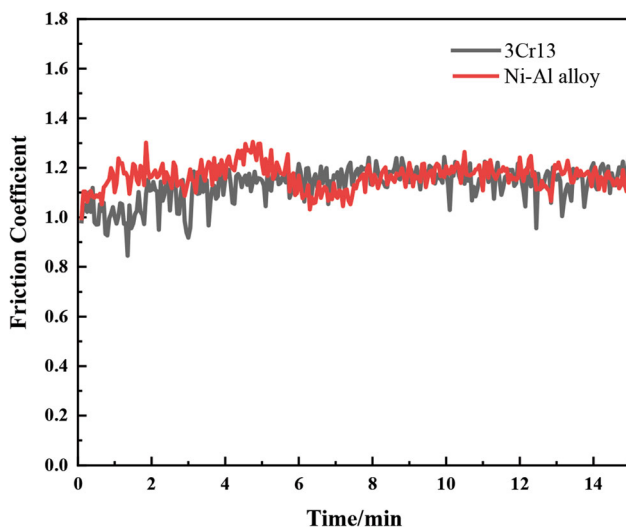


Fig. 11 Friction coefficients of the coatings at high temperature

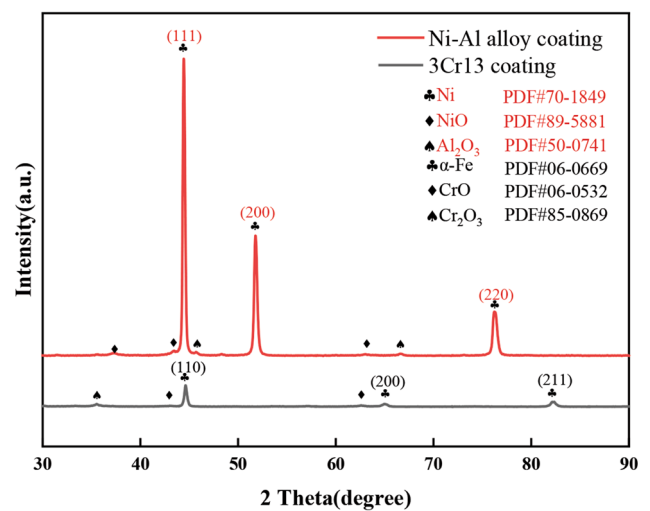


Fig. 12 XRD patterns of 3Cr13 (a), and Ni-Al (b) coatings after high-temperature friction testing

micro-peaks on the rough and uneven surfaces of the coatings. Friction generates a large amount of heat, which accumulates on the friction surface, leading to a high

temperature. Moreover, because the friction pair is located on the surface of the coating in air, oxide film is generated. In the friction test process, the oxide film acts as a

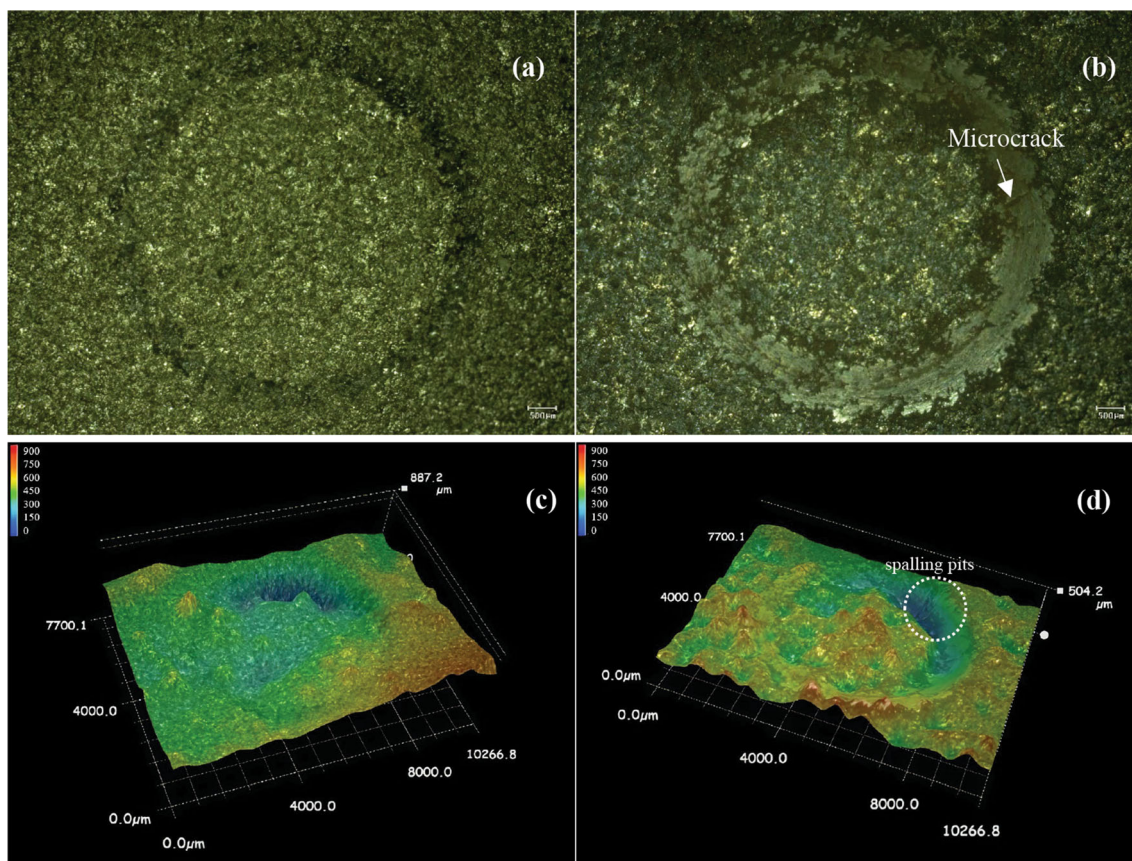


Fig. 13 Optical 2D and 3D micrographs of the scratches on the coatings after high-temperature friction testing: (a) 2D and (c) 3D micrographs of the Ni-Al coating, and (b) 2D and (d) 3D micrographs of the 3Cr13 coating

lubricant, helping to prevent further abrasion (Ref 49). According to Fig. 12, the oxide layer of the Ni-Al coating did not change after the high-temperature friction test, while high-temperature oxidation resistance of the coating is excellent. Thus, the Ni-Al coating (Fig. 13a and c) has a slighter high-temperature wear groove than the 3Cr13 coating, and there are no spalling pits. The martensite structure of the 3Cr13 coating is thermodynamically unstable at high temperature, and consequently the anti-wear performance will deteriorate (Ref 50). In Fig. 13(b) and (d), the scratch surface of the 3Cr13 coating appears to have an apparent layer structure and a plough groove. Spalling pits are an important manifestation of adhesive wear. The thermal and physical differences between the CrO or Cr₂O₃ film and the substrate, in conjunction with the friction force, can produce microcracks on the scratch surface. Microcracks propagate, penetrate, and rupture as the friction continues, causing debris and spalling pits to form.

Table 5 Results of simulated seawater immersion corrosion tests

Weight and corrosion rate	Ni-Al coating	3Cr13 coating
Before experiment, g	27.4783	23.9706
After experiment, g	27.4173	23.9064
Corrosion rate K, g/mm ² h	1.85×10^{-8}	2.15×10^{-8}

Corrosion Resistance

Simulated Seawater Immersion Corrosion

A 4-month simulated immersion test for the coating sample was conducted, as shown in Table 5. The corrosion rate of the Ni-Al coating and the 3Cr13 coating was 1.85×10^{-8} g/(mm² h) and 2.15×10^{-8} g/(mm² h), respectively. The corrosion rate of the Ni-Al coating is relatively slow, and therefore the corrosion resistance of Ni-Al coating is better than that of the 3Cr13 coating.

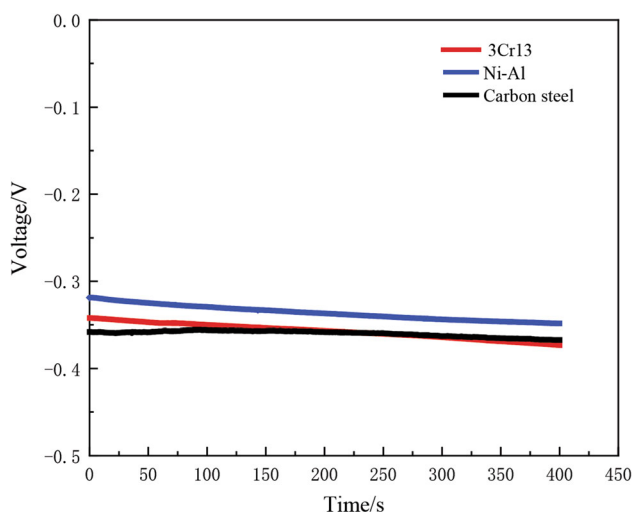


Fig. 14 Open circuit potential (OCP) curves of the coatings and the substrate

Electrochemical Corrosion

Figure 14 presents the OCP curves of the coatings and the substrate. The OCP values of the Ni-Al and 3Cr13 coatings are stable at about -0.33 and -0.35 V, respectively. The OCP value of the substrate is much more negative than that of the 3Cr13 coating, indicating that the Ni-Al deposit had higher corrosion resistance compared with the 3Cr13 coating and the substrate.

EIS measurements and Tafel polarization of the coatings and the substrate were carried out in 3.5% NaCl solution, as displayed in Fig. 15. The electrochemical corrosion data from Fig. 15(a), including the corrosion potential (E_{corr}) and the corrosion current density (I_{corr}), are presented in Table 6. The corrosion potentials of the substrate and the Ni-Al and 3Cr13 coatings are -0.421 , -0.570 , and -0.467 V, respectively. The corrosion potential of the Ni-Al coating shifted towards a more positive value, indicating that this coating exhibited better corrosion resistance than the others. In the passive region, the current density was relatively low and almost invariable, due to the formation of the passive films, which protected the coatings from corroding in the corrosive solution. The corrosion current densities of the Ni-Al and 3Cr13 coatings were 0.8×10^{-5} and 3.0×10^{-5} A cm^{-2} , respectively. In general, the higher the E_{corr} value, the better the chemical stability (Ref 51), and the smaller the I_{corr} value, the lower the corrosion rate. The Ni-Al coatings have a negative E_{corr} value, but the I_{corr} values are low in comparison to 3Cr13 coatings. In Fig. 15(b), the Nyquist plots of the coatings and the substrate are compressed semicircles. The semi-circle radius of the Ni-Al coating is larger than that of the substrate and the 3Cr13 coating. The larger the radius of the high-frequency capacitance loop, the better the

corrosion resistance of the coating. The Bode plots of the phase angle and impedance modulus are presented in Fig. 15(c) and (d). In the Bode plot for the phase angle at medium frequencies (Fig. 15c), there is a high broad peak for the Ni-Al and 3Cr13 coatings at 220° and 150° respectively, suggesting relatively high capacitive reactance value and hence good corrosion resistance of the coating. However, there is a broad peak for the substrate at 110° , observed in the Bode plot for the phase angle at low frequency, indicating poor corrosion resistance. It can be seen from Fig. 15(d) that the impedance modulus values of the coatings are almost stable in the low-frequency range. However, the impedance modulus value of the Ni-Al coating is slightly higher than that of the 3Cr13 coating, and the impedance modulus value of the substrate shows a gradual decrease. According to the above results, the corrosion resistance of the coatings was amended in the order of Ni-Al coating > 3Cr13 coating > carbon steel substrate.

Impedance spectra obtained for a given electrochemical system can be correlated to an equivalent circuit (Fig. 15e). Table 7 displays the impedance corrosion data of the simulated equivalent circuit, in which R_s represents the solution resistance in a 3.5 wt% NaCl solution, and $R_{\text{ct}}-C_{\text{dl}}$ represents the charge transfer resistance and the capacitance between the coating and the substrate. Moreover, R_{ct} electrochemical corrosion plays a vital role, which reflects the charge transfer process at the interface between the solution and the coating. The larger the R_{ct} value, the slower the corrosion rates (Ref 48). As shown in Table 7, the R_{ct} values of the Ni-Al coating, the 3Cr13 coating, and the substrate are 544.6, 341.5 and 328 $\Omega \text{ cm}^2$, respectively, indicating that the charge transfer process of the Ni-Al coating is slower than that of the 3Cr13 coating and the substrate carbon steel. Also, the C_{dl} value of the Ni-Al coating is much less than that of the 3Cr13 coating and the substrate carbon steel. Therefore, the Ni-Al alloy coating exhibited better corrosion resistance than the 3Cr13 coating and the substrate.

Galvanic Corrosion

The galvanic corrosion metals are the Ni-Al coating and the 3Cr13 coating. As displayed in Fig. 16, an electrochemical workstation was used to measure the corrosion voltage and current of the two groups of galvanic couples for 9 h. The corrosion current of the 3Cr13 coating is positive, but the corrosion current of Ni-Al coating is negative. After a long period of galvanic corrosion, the current of the 3Cr13 coating was close to zero. However, the current of the Ni-Al coating was unstable and increased toward the positive direction with increasing corrosion time. The chemical reaction formula of the corrosion for the 3Cr13 coating is (Ref 52, 53):

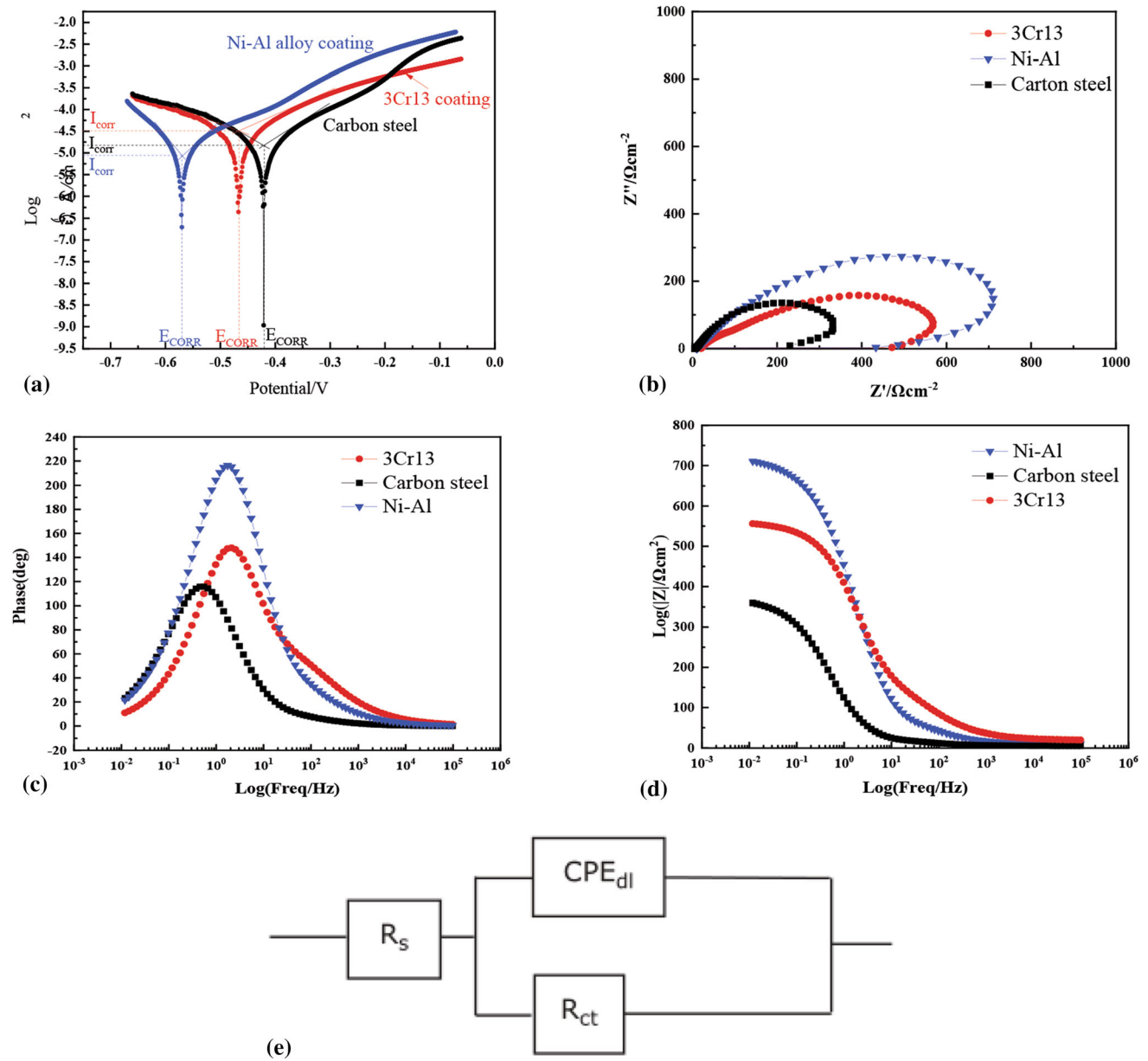


Fig. 15 Tafel polarization (a), Nyquist plots (b), Bode phase angles (c), impedance moduli (d), and fitting circuits (e) for the Ni-Al and 3Cr13 coatings and the substrate

Table 6 Electrochemical corrosion parameters of the coatings and the substrate

Parameters	Substrate	Ni-Al coating	3Cr13 coating
β_c	6.109	10.971	4.752
β_a	6.88	5.198	6.680
$I_{corr}, A/cm^2$	1.9×10^{-5}	0.8×10^{-5}	3.0×10^{-5}
E_{corr}, V	- 0.421	- 0.570	- 0.467
$R_p, \Omega cm^2$	237.1	1673.2	592.9
CR, mil/year	8.73	4.12	12.68

Table 7 Impedance fitted circuit data

Sample	$R_s, \Omega cm^2$	$R_{ct}, \Omega cm^2$	C_{dl}, F
Ni-Al coating	10.16	544.6	3.78×10^{-5}
3Cr13 coating	19.26	341.5	1.95×10^{-4}
Substrate	5.596	328	1.59×10^{-4}

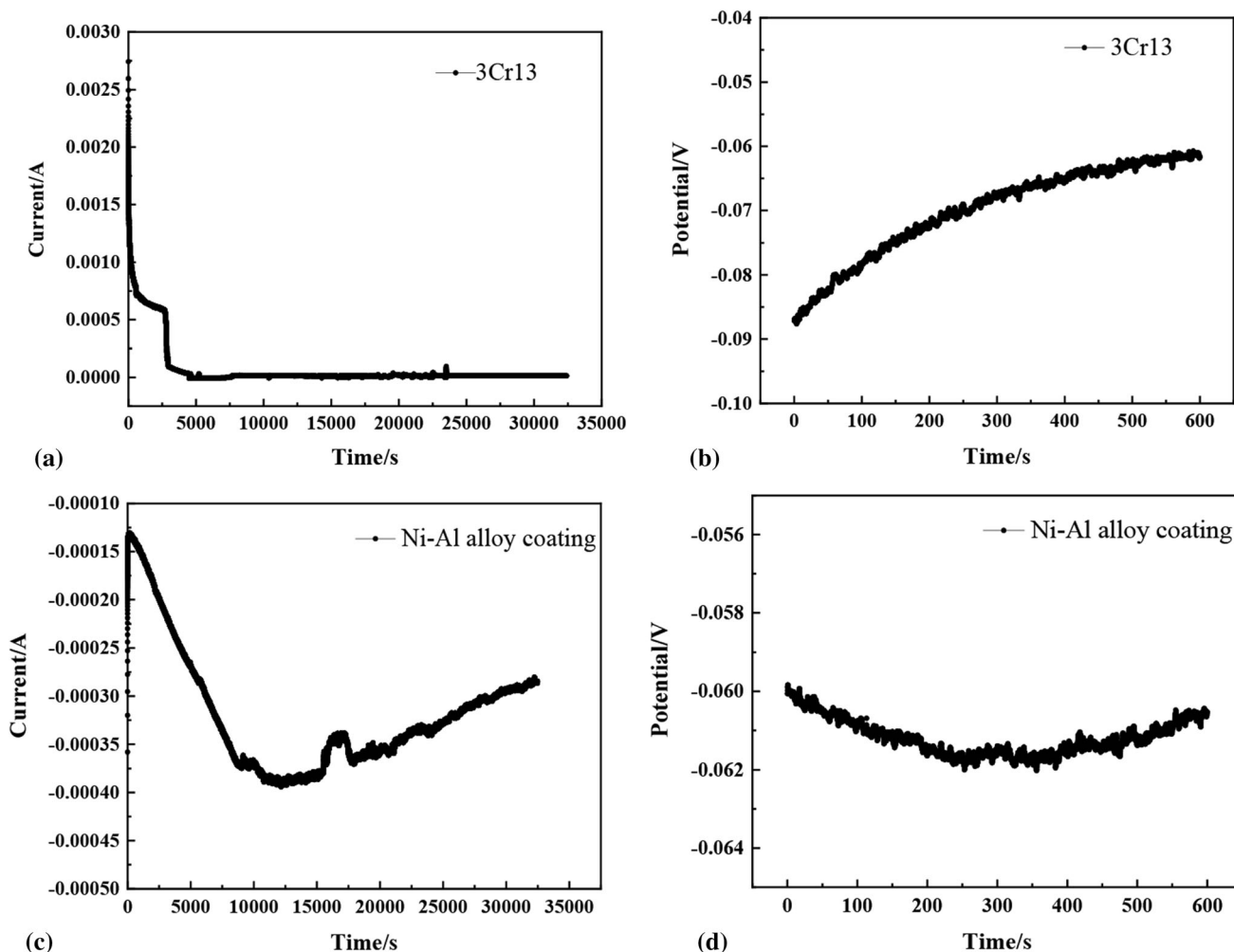
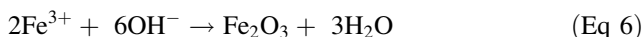
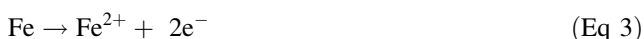


Fig. 16 Current and voltage of the galvanic couple for 9 h against running times: (a) current and (b) voltage of the 3Cr13 coating, (c) current and (d) voltage of the Ni-Al coating

Table 8 Average galvanic corrosion voltage of galvanic couples

Coating material	Galvanic corrosion voltage, V
3Cr13	- 0.336
Ni-Al	- 0.125



In Fig. 16(b) and (d), both coatings were corroded because their potentials displayed a negative voltage compared with the carbon steel. The galvanic corrosion voltage of the 3Cr13 coating gradually approaches the

positive voltage and has a gradually stable trend, while Ni-Al coating first shows a more negative voltage and then begins to approach the positive voltage. In Table 8, the corrosion potentials of the Ni-Al and 3Cr13 coatings are - 0.125 V and - 0.336 V, respectively. When the corrosion potential of the coating is more positive, the occurrence of a corrosion reaction becomes more difficult. Therefore, the corrosion resistance of the coating is good.

From Fig. 17(a), the surface of the 3Cr13 coating has been corroded and presents a pit-like morphology, while the surface of the Ni-Al coating is relatively flat with only a few scratches and a small amount of gully (Fig. 17b). According to the standard criteria (see Table 9), the contact sensitivity coefficients of the 3Cr13 and Ni-Al coatings reach grades D and E, respectively, indicating that the coatings should be protected when the coatings sprayed on the carbon steel were applied in the corrosion environment. The initial corrosion current density of the 3Cr13 coating is about $108 \mu\text{A cm}^{-2}$ (Fig. 16a), which is higher than that of

Fig. 17 Optical micrographs of: (a) the 3Cr13 coating and (b) the Ni-Al coating after galvanic corrosion testing ($\times 500$)

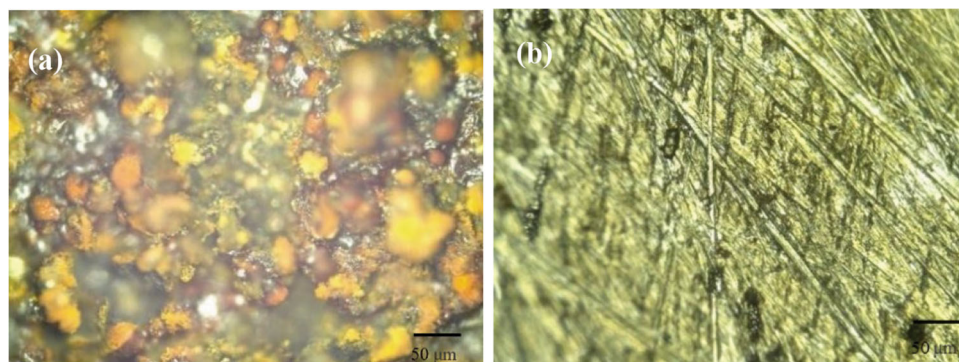
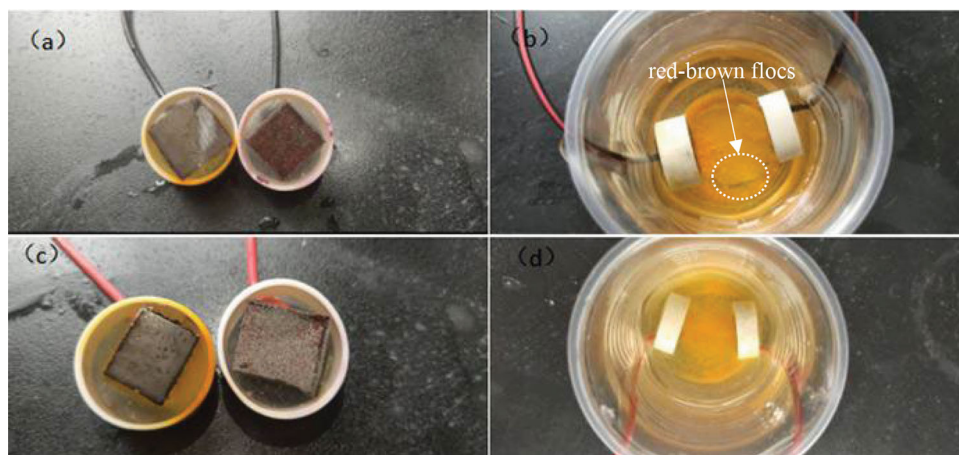


Table 9 Average current density and grade of galvanic couples

Galvanic couples	Current density, $\mu\text{A cm}^{-2}$	Grade	Conditions of use
3Cr13 coating, 1 h	108	E	Use after protection
3Cr13 coating, 9 h	8.67	D	Use after protection
Ni-Al coating, 1 h	15.4	E	Use after protection
Ni-Al coating, 9 h	37	E	Use after protection

Fig. 18 Digital images of the galvanic couples after galvanic corrosion of: (a, b) 3Cr13 coating couple, (c, d) Ni-Al coating couple



the Ni-Al coating of about $15.4 \mu\text{A cm}^{-2}$ (Fig. 16c). After a holding time of 9 h, the current density of the 3Cr13 coating decreased sharply to $8.67 \mu\text{A cm}^{-2}$, due to the formation of a passive layer on the top surface of the coating. In this case, the 3Cr13 coating was corroded and galvanic corrosion is no longer present.

Figure 18 shows digital images of the galvanic corrosion samples, which were exposed to galvanic corrosion immersion. In Fig. 18(a) and (c), both pairs of galvanic couples have corrosion on the top surface of the coating, and the corrosion products are colored red-brown. In Fig. 18(a), the surface of the 3Cr13 coating is covered by red-brown corrosion products, whereas the surface of the Ni-Al coating has less corrosion (Fig. 18c). The large potential difference between the two galvanic couples leads

to more serious corrosion on the base surface. Figure 18(b) and (d) displays the digital camera photos of the corrosion solution after galvanic corrosion for a period of time. The content of the red-brown floccules in solution for the 3Cr13 coating were significantly greater than those in solution for the Ni-Al coating, indicating that the surface of the 3Cr13 coating was seriously corroded. The galvanic corrosion experiment suggests that, under long-term galvanic corrosion, the galvanic couple formed between the 3Cr13 coating and the carbon steel has a higher tendency to be corroded than the galvanic couple formed between the Ni-Al alloy coatings and the carbon steel. Therefore, the corrosion resistance of the Ni-Al coating is better than that of the 3Cr13 coating.

Conclusions

Ni-Al and 3Cr13 coatings were prepared on carbon steel substrates by arc spraying. The microstructure, phase, microhardness, abrasion resistance, and corrosion resistance of the coatings were studied in detail. The main conclusions were as follows:

- (1) The thicknesses of the Ni-Al and 3Cr13 coatings were about 96.6 ± 4.6 and 177 ± 4.3 μm , respectively. The coatings show a lamellar structure. The 3Cr13 coating was composed of α -Fe phase and a small amount of CrO phase, the Ni-Al coating comprised a solid solution phase, and a small amount of NiO phase. The average surface roughnesses of the 3Cr13 coating, Ni-Al coating, and the polished substrate were 11, 14.4 and 0.13 μm , respectively. The Ni-Al coating had a porosity of 6.28%, while the 3Cr13 coating had a porosity of 5.22%. The microhardnesses of the Ni-Al coating, 3Cr13 coating, and the substrate were 162.8 ± 12.64 $\text{HV}_{0.5}$, 446.5 ± 24.89 $\text{HV}_{0.5}$, and 177.0 ± 2.26 $\text{HV}_{0.5}$, respectively.
- (2) At room temperature, the coatings were primarily subjected to abrasive and oxidative wear mechanisms. At the high temperature of 300 °C, the oxidation wear and adhesive wear were the predominant wear mechanisms. The abrasion resistance of the Ni-Al coating was better than that of the 3Cr13 coating at room temperature. Furthermore, the friction coefficient of the 3Cr13 coating was lower at high temperature than that of the Ni-Al coating, but the oxide film of the Ni-Al coating was more stable and there were no spalling pits after the high-temperature wear test.
- (3) The corrosion resistance of the Ni-Al coating was better than that of the 3Cr13 coating. The current density of galvanic corrosion of the 3Cr13 coating was $108 \mu\text{A cm}^{-2}$, while that of the Ni-Al coating was $37 \mu\text{A cm}^{-2}$. The galvanic corrosion resistance of the Ni-Al coating was larger than that of 3Cr13 coating. Therefore, the Ni-Al coating had good high temperature oxidation and abrasion resistance, simultaneously exhibiting good corrosion resistance in a corrosive solution contained chloride ions. The Ni-Al coating is suitable to be used as a protective barrier for boiler heater exchange pipelines, and for simultaneously enhancing the abrasion resistance and anticorrosion performance of the coating.

Acknowledgments The authors thank Dr. Ying Wang and Mr. Guang Yang from the Analysis and Testing Center, NERC Biomass of Changzhou University for discussion and helping in the surface

roughness and XRD measurement, respectively. Ms. Jiaqi Huang thanks to the funding of Postgraduate Research & Practice Innovation Program of Jiangsu Province (Grant no. SJCX22_1429).

Author contributions Dr. WW: planned, wrote, and supervised this work. YZ: prepared the coatings, co-wrote and edited this paper. Dr. WW: supervised master student Mr. YZ. JH, GS, YJ and GH: performed some experiments and some tests. Prof. YZ, Dr. WW, Dr. ZW, Dr. SF and Dr. PJ: performed and analyzed characterization of materials and samples. Prof. GO and Dr. WW discussed the corrosion experiments. All authors discussed the results and commented on the manuscript.

References

1. R. Chandraker, A. Kumar, and R. Kumar, Hot Corrosion Behaviour of Nickel Chromium Coating at Different Temperatures (800 and 900 °C) on SA213 T91 Boiler Steel Weldments, *Mater. Phys. Mech.*, 2012, **14**(1), p 11-30.
2. S.S. Chatha, H.S. Sidhu, and B.S. Sidhu, High-Temperature Hot Corrosion Behavior of NiCr and Cr_3C_2 -NiCr Coatings on T91 Boiler Steel in an Aggressive Environment at 750 °C, *Surf. Coat. Technol.*, 2012, **206**(19-20), p 3839-3850.
3. A. Mangla, V. Chawla, and G. Singh, Comparative Hot Corrosion Behavior of HVOF and Plasma Sprayed Ni_{20}Cr Coated T-22 Steel in Actual Coal Fired Boiler Environment, *J. Eng. Sci. Res.*, 2017, **4**(11), p 6-19.
4. G. Kaushal, H. Singh, and S. Prakash, High Temperature Corrosion Behaviour of HVOF-Sprayed Ni-20Cr Coating on Boiler Steel in Molten Salt Environment at 900 °C, *Int. J. Surf. Sci. Eng.*, 2011, **5**(5-6), p 415-433.
5. P. Daram, P.R. Munroe, and C. Banjongprasert, Microstructural Evolution and Nanoindentation of NiCrMoAl Alloy Coating Deposited by Arc Spraying, *Surf. Coat. Technol.*, 2020, **391**, p 125565.
6. V. Panwar, S. Shweta, V. Chawla, and N.K. Grover, A Comprehensive Review of Thermal Spray Coating for Coal-Fired Power Plants, *IJMERT*, 2017, **8**(7), p 1208-1217.
7. B. Formanek, K. Szymański, B. Szczucka-Lasota, and A. Włodarczyk, New Generation of Protective Coatings Intended for the Power Industry, *J. Mater. Process. Technol.*, 2005, **164-165**, p 850-855.
8. V. Boronenkov and Y. Korobov, *Fundamentals of Arc Spraying: Physical and Chemical Regularities*, Springer, Switzerland, 2016.
9. S. Matthews and M. Schweizer, Optimization of Arc-Sprayed Ni-Cr-Ti Coatings for High Temperature Corrosion Applications, *J. Therm. Spray Technol.*, 2013, **22**(4), p 538-550.
10. V.B. Chintada, R. Koona, and M. Bahubaldruni, State of Art Review on Nickel-Based Electroless Coatings and Materials, *J. Bio-Tribo-Corros.*, 2021, **7**(4), p 1-14.
11. G. Paczkowski, The New Old Way—High-Velocity Arc Spraying Allows New Perspectives & Process Diagnostics in Open Wire Arc Spraying. in *Colloquium High Velocity Oxy-Fuel Flame Spraying*, 9, C. Penszior, ed. by November 8-9, 2012 (Erding, Germany, Unterschleißheim: Gemeinschaft Thermisches Spritzen c/o Linde AG, 2012) p 139-150
12. H. Hu, L. Mao, S. Yin, H.L. Liao, and C. Zhang, Wear-Resistant Ceramic Coatings Deposited by Liquid Thermal Spraying, *Ceram. Int.*, 2022, **48**(22), p 33245-33255.
13. W.G. Chen, Z.X. Wang, G.L. Xu, W.T. Song, Y. Xie, L. Zhao, M.H. Xia, and W. Li, Friction and Anti-Corrosion Characteristics of Arc Sprayed Al+Zn Coatings on Steel Structures Prepared in Atmospheric Environment, *J. Mater. Res. Technol.*, 2021, **15**, p 6562-6573.

14. B. Zabala, A. Igartua, X. Fern´andez, C. Priestner, H. Ofner, O. Knaus, M. Abramczuk, P. Tribotte, F. Girot, E. Roman, and R. Nevshupa, Friction and Wear of a Piston Ring/Cylinder Liner at the Top Dead Centre: Experimental Study and Modelling, *Tribol. Int.*, 2017, **106**, p 23–33.
15. C.B. Tang, Z.L. Liu, D.D. Cui, L.H. Yu, J.Q. Xue, and X.Y. Yin, Enhancing the Stability and Electrocatalytic Activity of Ti-Based PbO₂ Anodes by Introduction of an Arc-Sprayed TiN Interlayer, *Electrochim. Acta*, 2021, **399**, p 139398.
16. A. Sato, Y.L. Chiu, and R.C. Reed, Oxidation of Nickel-Based Single Crystal Superalloys for Industrial Gas Turbine Applications, *Acta Mater.*, 2011, **59**(1), p 225–240.
17. N.P. Padture, M. Gell, and E.H. Jordan, Thermal Barrier Coatings for Gas-Turbine Engine Applications, *Science*, 2002, **296**, p 280–284.
18. K. Szymański, A. Hernas, and G. Moskal, Thermally Sprayed Coatings Resistant to Erosion and Corrosion for Power Plant Boilers—A Review, *Surf. Coat. Technol.*, 2015, **268**, p 153–164.
19. M. Hetmańczyk, L. Swadba, and B. Mendala, Advanced Materials and Protective Coatings in Aero-Engines Application, *J. Achiev. Mater. Manuf.*, 2007, **24**(1), p 372–381.
20. S. Kuroda, T. Fukushima, M. Sasaki, and T. Kodama, Microstructure and Corrosion Resistance of HVOF Sprayed 316L Stainless Steel and Hastelloy C Coatings, *Mater. Trans.*, 2002, **43**(12), p 3177–3183.
21. A. Hussinger, Analyzing the corrosion resistance of Ni-shield 200 coatings at different temperatures when exposed to sulphuric acid. BS in Materials Engineering (California Polytechnic State University, 2012)
22. P.L. Fauchais, J.V.R. Heberlein, and M.I. Boulos, *Thermal Spray Fundamentals: From Powder to Part*, Springer, New York, USA, 2014.
23. S. Kant, M. Kumar, V. Chawla, and S. Singh, Study of High-Temperature Oxidation Behavior of Wire Arc Sprayed Coatings, *Mater. Today*, 2020, **21**, p 1741–1748.
24. K. Yang, X.M. Zhou, H.Y. Zhao, and S.Y. Tao, Microstructure and Mechanical Properties of Al₂O₃-Cr₂O₃ Composite Coatings Produced by Atmospheric Plasma Spraying, *Surf. Coat. Technol.*, 2011, **206**(6), p 1362–1371.
25. M.A. Zavareh, A. Sarhan, B.A. Razak, and W.J. Basirun, The Tribological and Electrochemical Behavior of HVOF-Sprayed Cr₃C₂-NiCr Ceramic Coating on Carbon Steel, *Ceram. Int.*, 2015, **41**(4), p 5387–5396.
26. M. Bloomfield, K. Christofidou, and N. Jones, Effect of Co on the Phase Stability of CrMnFeCo_xNi High Entropy Alloys Following Long-Duration Exposures at Intermediate Temperatures, *Intermetallics*, 2019, **114**, p 106582.
27. W. Bach, Z. Babiak, T. Rothbard, and B. Formanek, Properties of plasma and D-gun sprayed metal-matrix composite (MMC) coatings based on ceramic hard particle reinforced Fe-, Ni-aluminide matrix, in *Thermal spray 2003: Advancing the science and applying the technology* ed by Marple BR, Moreau C, editors, May 5–8, 2003 (Orlando, FL, ASM Thermal Spray Society, 2003)
28. T. Keller, N. Margadant, and T. Pirling, Residual Stress Determination in Thermally Sprayed Metallic Deposits by Neutron Diffraction, *Mater. Sci. Eng. A*, 2004, **373**(1–2), p 33–44.
29. Y. Tian, C. Lu, Y. Shen, and X.M. Feng, Microstructure and Corrosion Property of CrMnFeCoNi High Entropy Alloy Coating on Q235 Substrate Via Mechanical Alloying Method, *Surf. Interfaces*, 2019, **15**, p 135–140.
30. S.K. Rai, A. Kumar, and V. Shankar, Characterization of Microstructures in Inconel 625 Using x-ray Diffraction Peak Broadening and Lattice Parameter Measurements, *Scr. Mater.*, 2004, **51**(1), p 59–63.
31. A. Kotvickii, G.S. Kraynova, A.M. Frolov, V. Ivanov, and S.V. Plotnikov, Influence of Fe-Co Ratio and Ni, Cr Dopants on Structural Evolution of Metallic Amorphous Alloys, *Solid State Phenom.*, 2014, **215**, p 179–184.
32. M. Kouřil, P. Novak, and M. Bojko, Limitations of the Linear Polarization Method to Determine Stainless Steel Corrosion Rate in Concrete Environment, *Cem. Concr. Compos.*, 2006, **28**(3), p 220–225.
33. I.C. Park and S.J. Kim, Corrosion Behavior in Seawater of Arc Thermal Sprayed Inconel 625 Coatings with Sealing Treatment, *Surf. Coat. Technol.*, 2017, **325**, p 729–737.
34. S.F. Bonabi, F. Ashrafzadeh, and A. Sanati, Structure and Corrosion Behavior of Arc-Sprayed Zn-Al Coatings on Ductile Iron Substrate, *J. Therm. Spray Technol.*, 2018, **27**(3), p 524–537.
35. X. Pang, K. Gao, and F. Luo, Annealing Effects on Microstructure and Mechanical Properties of Chromium Oxide Coatings, *Thin Solid Films*, 2008, **516**(15), p 4685–4689.
36. D. Landolt, S. Mischler, and M. Stemp, Electrochemical Methods in Tribocorrosion: A Critical Appraisal, *Electrochim. Acta*, 2001, **46**(24–25), p 3913–3929.
37. A. Ganvir, N. Curry, S. Björklund, N. Markocsan, and P. Nylén, Characterization of Microstructure and Thermal Properties of YSZ Coatings Obtained by Axial Suspension Plasma Spraying (ASPS), *J. Therm. Spray Technol.*, 2015, **24**(7), p 1195–1204.
38. M.D. Mathew, P. Parameswaran, and K.B.S. Rao, Microstructural Changes in Alloy 625 During High-Temperature Creep, *Mater. Charact.*, 2008, **59**(5), p 508–513.
39. A.J. Goodfellow, E.I. Galindo-Nava, K.A. Christofidou, N.G. Jonesa, C.D. Boyerb, T.L. Martinc, P.A.J. Bagotc, M.C. Hardyd, and H.J. Stonea, The Effect of Phase Chemistry on the Extent of Strengthening Mechanisms in Model Ni-Cr-Al-Ti-Mo Based Superalloys, *Acta Mater.*, 2018, **153**, p 290–302.
40. F.K. Thomas, P. Thilo, and M. Nikolaus, Residual Stress Determination in Thermally Sprayed Metallic Deposits by Neutron Diffraction, *Mater. Sci. Eng.*, 2004, **373**(1), p 33–44.
41. Y. Huang and X. Peng, The Promoted Formation of an α -Al₂O₃ Scale on a Nickel Aluminide with Surface Cr₂O₃ Particles, *Corros. Sci.*, 2016, **112**, p 226–232.
42. E.R. Sampson, Thermal Spray Coatings for Corrosion Protection: An Overview, *Mater. Perform.*, 1997, **38**(12), p 27–30.
43. B.A. Pint, P.F. Tortorelli, and I.G. Wright, Effect of Cycle Frequency on High-Temperature Oxidation Behavior of Alumina-Forming Alloys, *Oxid. Met.*, 2002, **58**(1–2), p 73–101.
44. R. Starosta, Properties of Thermal Spraying Ni-Al Alloy Coatings, *Adv. Mater. Sci.*, 2009, **9**(1), p 30–40.
45. R.G. Davies, Influence of Martensite Composition and Content on the Properties of Dual-Phase Steels, *Mater. Trans. A*, 1978, **9**(5), p 671–679.
46. H.L. Tian, S.C. Wei, and Y.X. Chen, Adhesive Strength and Abrasive Property of Fe Based Composite Coating Deposited by High Velocity Arc Spraying, *Mater. Res. Innov.*, 2014, **18**(S2), p 363–367.
47. J.J. Kang, C.B. Wang, H.D. Wang, B.S. Xu, J.J. Liu, and G.L. Li, Characterization and Tribological Properties of Composite 3Cr13/FeS Layer, *Surf. Coat. Technol.*, 2009, **203**(14), p 1927–1932.
48. S. Khireche, D. Boughrara, A. Kadri, L. Hamadou, and N. Benbrahim, Corrosion Mechanism of Al, Al-Zn and Al-Zn-Sn Alloys in 3 wt% NaCl Solution, *Corros. Sci.*, 2014, **87**, p 504–516.
49. H. Berns and A. Fischer, Tribological Stability of Metallic Materials at Elevated Temperatures, *Wear*, 1993, **162**, p 441–449.
50. X. Ren, F. Wang, and W. Xin, High-Temperature Oxidation and Hot Corrosion Behaviors of the NiCr-CrAl Coating on A Nickel-Based Superalloy, *Surf. Coat. Technol.*, 2005, **198**(1–3), p 425–431.

51. W.P. Wu, J.Q. Huang, and J. Nather, Texture Orientation, Morphology, and Performance of Nanocrystalline Nickel Coatings Electrodeposited from a Watts-Type Bath: Effects of H_3BO_3 Concentration and Plating Time, *Surf. Coat. Technol.*, 2021, **424**, p 127648.
52. T. Poornima, J. Nayak, and A.N. Shetty, 3,4-Dimethoxybenzaldehydethiosemicarbazone as Corrosion Inhibitor for Aged 18 Ni 250 Grade Maraging Steel in 0.5M Sulfuric Acid, *J. Appl. Electrochem.*, 2011, **41**(2), p 223-233.
53. A. Kotvitckii, G.S. Kraynova, A.M. Frolov, I. Vitaly, and S.P. Vladimir, Influence of Fe-Co Ratio and Ni, Cr Dopants on Structural Evolution of Metallic Amorphous Alloys, *Solid State Phenom.*, 2014, **215**, p 179-184.

Publisher's Note Springer Nature remains neutral with regard to jurisdictional claims in published maps and institutional affiliations.

Springer Nature or its licensor (e.g. a society or other partner) holds exclusive rights to this article under a publishing agreement with the author(s) or other rightsholder(s); author self-archiving of the accepted manuscript version of this article is solely governed by the terms of such publishing agreement and applicable law.